AGU PUBLICATIONS

Geophysical Research Letters

RESEARCH LETTER
10.1002/2017GL076085

Key Points:
- The 2017 M_w 8.2 Chiapas normal faulting earthquake beneath the Tehuantepec gap involved lithospheric-transecting rupture of the thin Cocos slab
- Seismic, tsunami, and GPS data indicate that the rupture extended ~100 km unilaterally to the northwest along strike and from ~30 to 70 km in depth
- Relative to megathrust earthquakes, subduction zone intraslab faulting is more energetic, resulting in strong ground shaking for the 2017 event

Supporting Information:
- Supporting Information S1
- Movie S1

Correspondence to:
L. Ye,
lingling@gps.caltech.edu

Citation:
Ye, L., Lay, T., Bai, Y., Cheung, K. F., & Kanamori, H. (2017). The 2017 M_w 8.2 Chiapas, Mexico, earthquake: Energetic slab detachment. *Geophysical Research Letters*, *44*. https://doi.org/10.1002/2017GL076085

Received 19 OCT 2017
Accepted 22 NOV 2017
Accepted article online 4 DEC 2017

The 2017 M_w 8.2 Chiapas, Mexico, Earthquake: Energetic Slab Detachment

Lingling Ye[1,2], Thorne Lay[3], Yefei Bai[4], Kwok Fai Cheung[4], and Hiroo Kanamori[2]

[1]Guangdong Provincial Key Lab of Geodynamics and Geohazards, School of Earth Sciences and Engineering, Sun Yat-sen University, Guangzhou, China, [2]Seismological Laboratory, California Institute of Technology, Pasadena, CA, USA, [3]Department of Earth and Planetary Sciences, University of California, Santa Cruz, CA, USA, [4]Department of Ocean and Resources Engineering, University of Hawai'i at Mānoa, Honolulu, HI, USA

Abstract On 8 September 2017, a great (M_w 8.2) normal faulting earthquake ruptured within the subducting Cocos Plate ~70 km landward from the Middle American Trench beneath the Tehuantepec gap. Iterative inversion and modeling of teleseismic and tsunami data and prediction of GPS displacements indicate that the steeply dipping rupture extended ~180 km to the northwest along strike toward the Oaxaca coast and from ~30 to 70 km in depth, with peak slip of ~13 m. The rupture likely broke through the entire lithosphere of the young subducted slab in response to downdip slab pull. The plate boundary region between the trench and the fault intersection with the megathrust appears to be frictionally coupled, influencing location of the detachment. Comparisons of the broadband body wave magnitude (m_B) and moment-scaled radiated energy (E_R/M_0) establish that intraslab earthquakes tend to be more energetic than interplate events, accounting for strong ground shaking observed for the 2017 event.

Plain Language Summary A large earthquake ruptured in the subducting Cocos Plate that underthrusts Mexico and Central America offshore of Chiapas, in southern Mexico. Analysis of seismic waves, deepwater tsunami recordings, and onshore geodetic displacements establishes that the rupture was on a steeply dipping fault plane and that the slip extended across the entire underthrust lithosphere, partially detaching the deeper slab. The event is located beneath the continental shelf, and there is a narrow zone of the megathrust from the Middle American Trench to where this event reached the plate boundary that appears to have frictional coupling, which likely influenced the location of the slab detachment. The event radiated stronger short-period seismic waves than typical of comparable size events on subduction zone plate boundaries, producing severe damage in Oaxaca and Chiapas.

1. Introduction

Along the stretch of the Middle American Trench offshore of southern Mexico from 94°W to 96°W, the Tehuantepec Ridge is subducting at ~7.5 cm/yr (Figure 1). The dip of the underthrust Cocos slab transitions from shallowly dipping beneath Mexico to the northwest to steeply dipping beneath Central America to the southeast (Ponce et al., 1992). There is no record of a confidently identified large underthrusting earthquake on the plate boundary in this region, so it has been designated as the Tehuantepec gap for many decades (e.g., Kelleher & McCann, 1976; Kelleher et al., 1973; Nishenko, 1991; Singh et al., 1981), with very uncertain seismic potential. This region was struck by a large earthquake on 8 September 2017 (15.022°N, 93.899°W, 47.4 km deep, 04:49:19.2 UTC, U.S. Geological Survey-National Earthquake Information Center (USGS-NEIC), last updated on 27 October 2017, https://earthquake.usgs.gov/earthquakes/eventpage/us2000ahv0#origin). Rather than being a plate boundary thrust event to fill the seismic gap, its faulting mechanism and depth indicate an intraslab normal fault rupture. The moment magnitude estimates from the USGS-NEIC (M_{ww} 8.1) and the global centroid moment tensor (gCMT) Project (M_w 8.2; http://www.globalcmt.org/CMTsearch.html) and the ~200 km long distribution of early aftershocks indicate a rare great intraslab earthquake located beneath the broad continental slope offshore of southern Mexico (Figure 1). The hypocenter estimate in the Mexican Servicio Sismológico Nacional (SSN) catalog (14.85°N, 94.11°W, 58 km deep, Servicio Sismológico Nacional, National Autonomous University of Mexico, http://www.ssn.unam.mx/, SSN, 2017) is located about ~30 km southwest of the USGS-NEIC location (Figure 1).

Shaking from the earthquake was devastating in southern Mexico, with at least 98 fatalities, mostly in Oaxaca, and 41,000 homes damaged. Peak tsunami waves of 1 to 1.75 m amplitude were recorded at Salina Cruz and

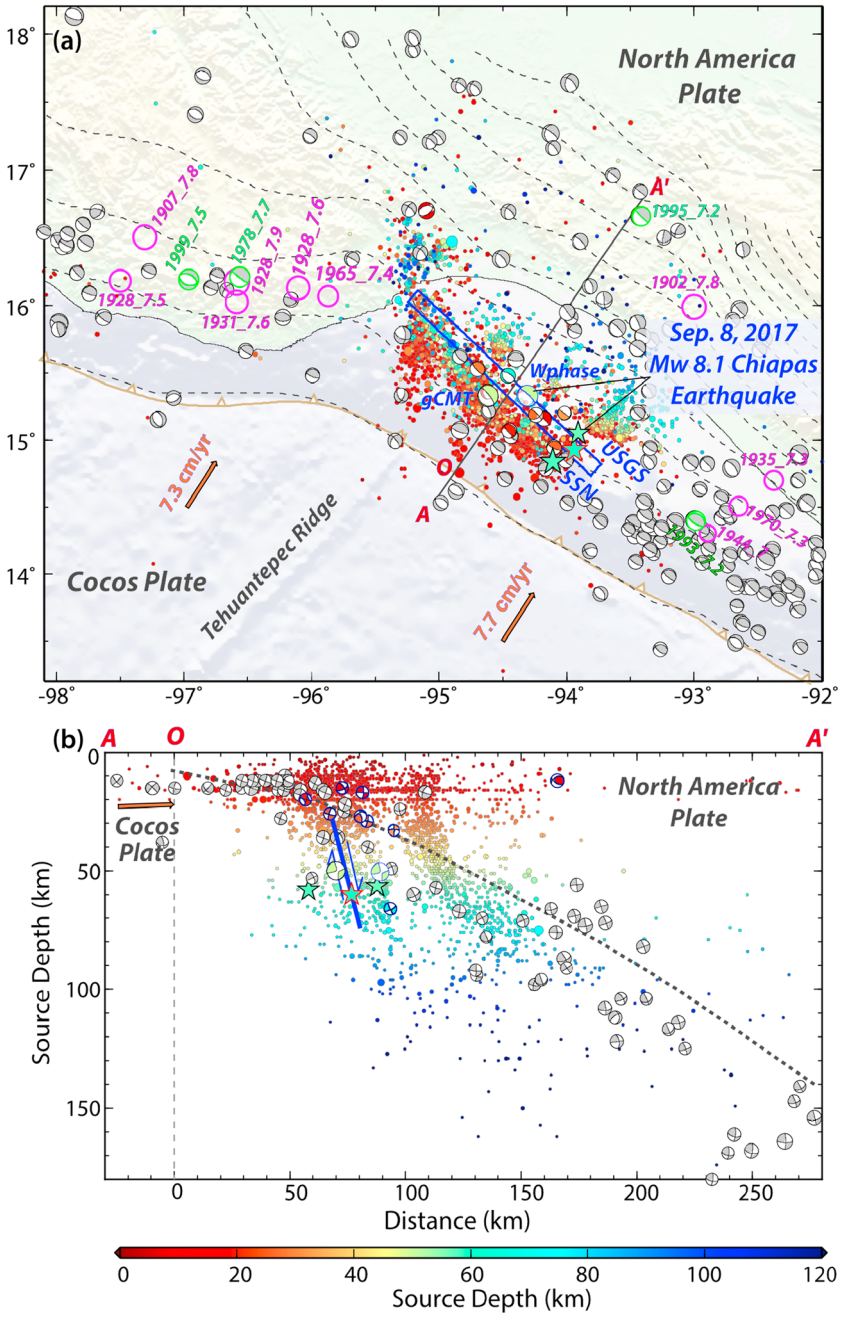

Figure 1. Tectonic environment and seismicity around the 2017 M_w 8.2 Chiapas earthquake. (a) Large earthquakes (M ~7+) from 1900 to 1976 from the USGS-NEIC catalog (magenta circles), along with gCMT solutions for M5+ events from 1976 to 2017 (gray focal mechanisms). Stars show epicenters of the 2017 Chiapas mainshock from USGS-NEIC, SSN, and our relocation from regional P arrivals. Green focal mechanisms show gCMT and W phase solutions. Blue rectangle indicates the slip region of our preferred slip model. Aftershocks with $M \geq 3.5$ from SSN (circles), along with available gCMT solutions, are color coded with source depth. The dashed curves show slab surface depths from model slab 1.0 (Hayes et al., 2012) with 20 km increments. Arrows indicate the Cocos Plate motion relative to a fixed North American Plate from model MORVEL (DeMets et al., 2010). (b) Depth profile of the mainshock, aftershock sequence, and gCMT focal mechanisms along profile A–A′ (azimuth 35°) within distances of ±175 km. The bold blue line indicates the approximate depth extent of the mainshock from our preferred slip model. The dashed gray curve shows the slab surface along profile A–A′.

in Chiapas. The offshore faulting location prevented even more severe shaking damage. Large shallow (<70 km deep) intraslab normal faulting has previously struck beneath Mexico inland, causing major destruction, such as in 1858 (M ~7.7; Singh et al., 1996), 1907 (Oaxaca, M ~7.6), 1931 (Oaxaca, M ~7.6; Singh et al., 1985), 1957 (Guerrero, M ~7.6), and 1999 (Oaxaca, M_w 7.5; Singh et al., 2000), as well as beneath the broader offshore continental slope along Guatemala (1957, M ~7.7) and El Salvador (2001, M_w 7.7; Vallée et al., 2003).

The 2017 event is the largest intraslab earthquake documented along the Mexican subduction zone, and it is challenging to evaluate the seismic potential for such events given that the strain budgets in the slab are poorly known. Temporal patterns of intraslab seismicity have been examined for coupled and uncoupled subduction zones (Astiz & Kanamori, 1986; Astiz et al., 1988; Christensen & Ruff, 1988; Dmoska et al., 1988; Lay et al., 1989; Mikumo et al., 2002; Ye et al., 2012). For weakly coupled regions, great intraslab normal faulting may occur near the trench or in the outer rise, such as the 1977 M_w 8.3 Sumba earthquake (Lynnes & Lay, 1988; Spence, 1986), or after a preceding megathrust event has ruptured the shallow coupled zone, as for the 1933 M_w 8.4 Sanriku earthquake (Kanamori, 1971) or the 2007 Kuril M_w 8.1 earthquake (e.g., Lay et al., 2009). If there is strong coupling of the megathrust that has not recently failed, great intraslab normal faulting may occur downdip of the coupled zone, as for the 1977 M_w 8.1 Tonga earthquake (Christensen & Lay, 1988).

The Tehuantepec Ridge has significant bathymetric expression, and the buoyant ridge intersects the coast where there is a major landward shift of the coastline and a broad submerged continental shelf. GPS stations in Chiapas are thus located at large distance from the shallow megathrust, unlike along Oaxaca where the offshore distance to the trench is small. The plate boundary in the Tehuantepec gap has relatively few interplate thrust fault events in the gCMT catalog (Figures 1 and S1 in the supporting information), with most locating seaward of the aftershock region of the 2017 event. There are more interplate thrusting events along the megathrust along Oaxaca to the northwest and offshore of the southernmost Chiapas coast east of 94°W. This region is also tectonically complicated by the northwestward extent of the Caribbean Plate and the oblique trend of the Caribbean-North American plate boundary through central Guatemala and offshore over the region of the 2017 rupture (e.g., Franco et al., 2012). The Caribbean Plate appears to be leaving a forearc block behind as it moves eastward, complicating the upper plate deformation pattern. Franco et al. (2012) allow for this and infer fairly high interplate coupling, >0.6, offshore of Chiapas as far west as 95.5°W, spanning the region above the 2017 rupture zone, in contrast to relatively low coupling to the southeast offshore Guatemala and El Salvador.

The rupture characteristics of the 2017 Chiapas earthquake are determined here to evaluate tectonic implications of this event and to address the severity of the strong shaking associated with the source radiation.

2. Analysis of the Source Process

Global long-period *W* phase data are inverted for a point source representation of the 2017 earthquake to constrain the faulting geometry, centroid depth, and seismic moment (Kanamori & Rivera, 2008). We use 182 channels from 71 Federation of Digital Seismic Network stations filtered in the frequency band of 2 to 5 mHz. The best double couple for the solution has strike 313°, dip 77.7°, and rake −95.5°, with seismic moment of 2.57×10^{21} Nm (M_w 8.21), a 26.0 s centroid time shift for an assumed symmetric triangular source time function, and a centroid location of 15.340°N, 94.309°W at 50.5 km depth (Figure S2). The centroid depth resolution for the *W* phase inversion is limited, so we enhance the sensitivity by evaluating the misfit in the predicted fundamental mode of Rayleigh waves that follows the *W* phase window for vertical component recordings using the *W* phase inversion solutions for specified depths. The Rayleigh wave misfit is also minimized at 50.5 km, with a broad region of low misfit from 45 to 65 km (Figure S2).

Given the tendency for USGS-NEIC locations to be biased in the slab dip direction for subduction zones (Figure S1c), we measure the first arrival times from regional seismograms to relocate the hypocenter. A grid search indicates an optimal location at 14.940°N, 93.940°W (Figure S3), which is between the initial USGS location (subsequently updated to nearer our preferred location) and the SSN location, placing the hypocenter below the shelf break (Figures 1 and S3). The depth is not resolved in the relocation, and we fix it at 60 km, similar to the other solutions.

For the relocated hypocenter, we perform a teleseismic short-period (0.5–2.0 s) *P* wave backprojection for data in westernmost North America (Figure S4), using the method of Xu et al. (2009). The resulting image indicates unilateral rupture propagation toward the northwest, extending into Oaxaca, with overall maximum rupture speed of ~3 to 4 km/s. We found that backprojections for seismic networks in eastern North America and Europe or for a global configuration did not provide robust images.

Guided by the faulting geometry from the *W* phase inversion, our relocated hypocenter, and the kinematic constraints from the backprojection, we invert for finite-fault rupture models using teleseismic broadband

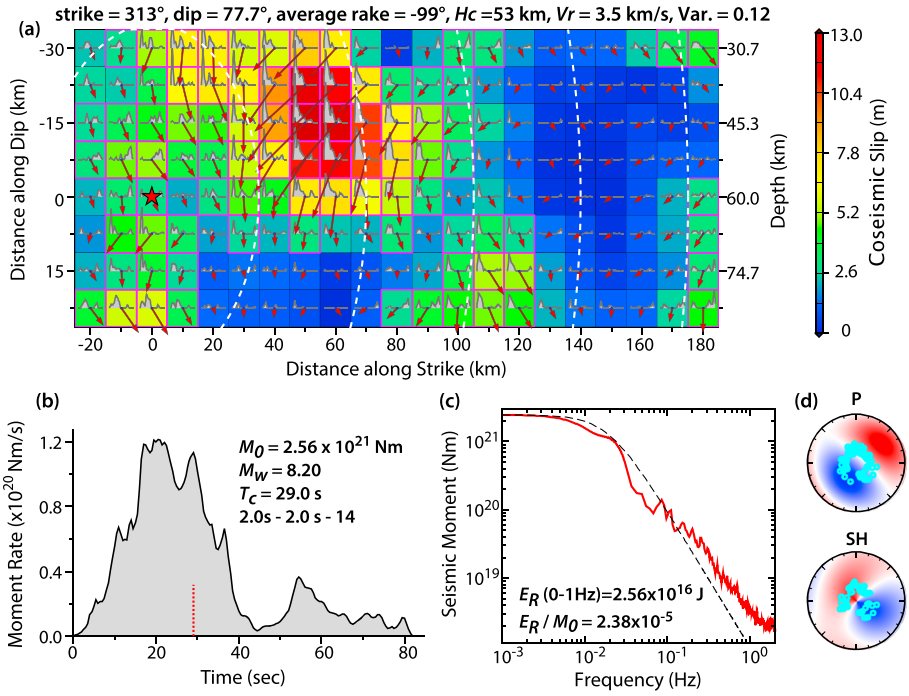

Figure 2. Finite-fault slip model inverted from teleseismic *P* and *SH* waves for the 2017 Chiapas earthquake. (a) The slip distribution with arrows indicating average rake of each subfault, and slip magnitude being color coded, and 10 s isochrones for the expanding rupture front (white dashed curves). (b) The moment rate function, seismic moment, and centroid time. (c) The average source spectrum (red) and a reference ω^{-2} spectrum (dashed line) with assumed stress parameter of 3 MPa and shear wave speed of 3.75 km/s. (d) Radiation patterns of teleseismic *P* and *SH* waves from the average double-couple focal mechanism. Cyan dots indicate the positions sampled by 74 *P* waves and 49 *SH* waves used in the inversions.

P wave displacements and *SH* wave ground velocities (Figure 3) using linear least squares inversion based on Hartzell and Heaton (1983) and Kikuchi and Kanamori (1992), as updated by Ye et al. (2016a). We use a planar fault extending asymmetrically toward the northwest, parameterizing each subfault to 10 km along strike and 7.5 km along dip, with a source time function having fourteen 2 s rise time triangles offset by 2 s each, allowing up to 30 s subfault durations. The teleseismic data can be fit very well for predominantly unilateral models with maximum rupture expansion velocities of 3 to 4 km/s and total rupture lengths of 160 km or longer, for the USGS, SSN, or our preferred source locations. To improve the constraint on the absolute location of the faulting and the overall rupture length, we model deepwater tsunami recordings and a preliminary open data set of coseismic displacements from daily GPS records (Nevada Geodetic Laboratory, http://geodesy.unr.edu/). Figure 2 shows the final rupture model that we obtain, and Figure 3 shows the fit to the teleseismic observations for this model.

We obtain this final model by iterative modeling of five ocean bottom pressure sensor recordings from NOAA Deep-Ocean Assessment and Reporting of Tsunami (DART) buoy stations (Figure 4b), which recorded very clear deepwater tsunami waveforms. In modeling the tsunami recording we use NEOWAVE, a shock-capturing nonhydrostatic model based on the staggered finite-difference formulation (Yamazaki, Cheung, et al., 2011; Yamazaki et al., 2009). The governing, nonlinear shallow water equations are coupled with a pressure Poisson equation for the depth-averaged vertical velocity, which accounts for weakly dispersive tsunami waves. The vertical velocity term also describes the time-varying deformation of the seafloor making the calculation fully consistent with the kinematic finite-fault slip model. Two 2-way nested grid levels are used to represent the 30 arc sec GEBCO bathymetry near the coastal source region and 2 arc min bathymetry over the eastern Pacific.

We follow an iterative modeling strategy similar to prior successful applications (e.g., Bai et al., 2017; Lay et al., 2013 Yamazaki, Lay, et al., 2011), inverting the seismic data for a finite source model, predicting the tsunami observations, deducing necessary modifications of the underconstrained seismic inversion parameters (fault dimensions and absolute fault placement) and iterating to convergence on a self-consistent

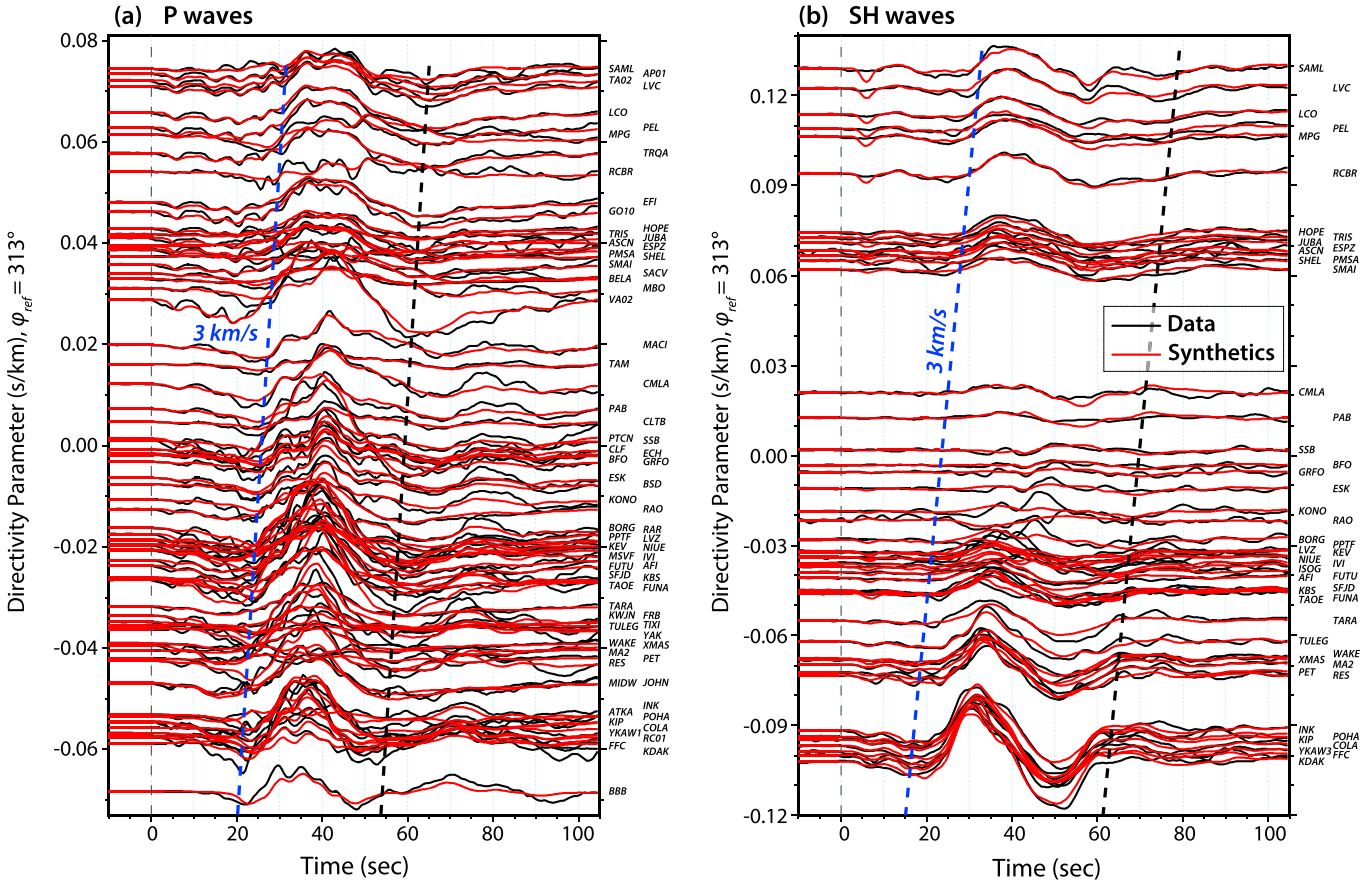

Figure 3. Comparison between observed (black) and synthetic (red) teleseismic (a) *P* displacement and (b) *SH* velocity waveforms from our preferred slip model, plotted as a function of directivity parameter relative to the fault strike direction. The blue dashed lines show unilateral rupture to the northwest along the fault strike direction with a speed of 3.0 km/s.

source representation that provides good fit to both sets of observations. We focus on the distribution of slip along strike and the absolute placement of the model. The shallow continental shelf is effective in trapping tsunami energy. The initial arrivals at the DART stations primarily come from the uplift on the continental slope (Figure 4a). The stations provide 180° coverage of the tsunami to constrain the fault placement (Figure 4b). Using the initial USGS-NEIC location, we found very poor prediction of the tsunami waveforms and deduced that the source must locate closer to the shelf break. We also found poor predictions of the tsunami for the SSN location. Using our relocated hypocenter from regional travel times in between the USGS-NEIC and SSN locations (Figure S3), we find significant improvement in the tsunami waveform fits (Figure 4c).

A suite of models for varying choices of strike, dip, hypocenter, fault length, rupture speed, and subfault duration defines the range of parameters compatible with both seismic and tsunami observations. Rupture models with fault lengths <150 km provide satisfactory fits to both data sets. However, the GPS displacements for stations in Oaxaca provide additional constraints on the northwestward extent of faulting (Figure 4a). We therefore seek models consistent with all three data types by extending the rupture to near the Oaxaca coast, matching the strength and direction of the displacements at stations OXTH, OXUM, TNSJ, TNNP, and TNCY using the elastic half-space solution of Okada (1985). The rupture model in Figure 2, obtained mainly from seismic inversion, predicts the horizontal displacements well for the Oaxaca stations (Figure 4a) and gives excellent fits to the seismic data accounting for 88% of the signal power (Figure 3) and to the tsunami waveforms (Figure 4c).

The preferred model has a rupture expansion speed of 3.5 km/s, resolved to about ±0.5 km/s, and a fault extending 185 km northwestward from our relocated hypocenter to below the Oaxaca coastline

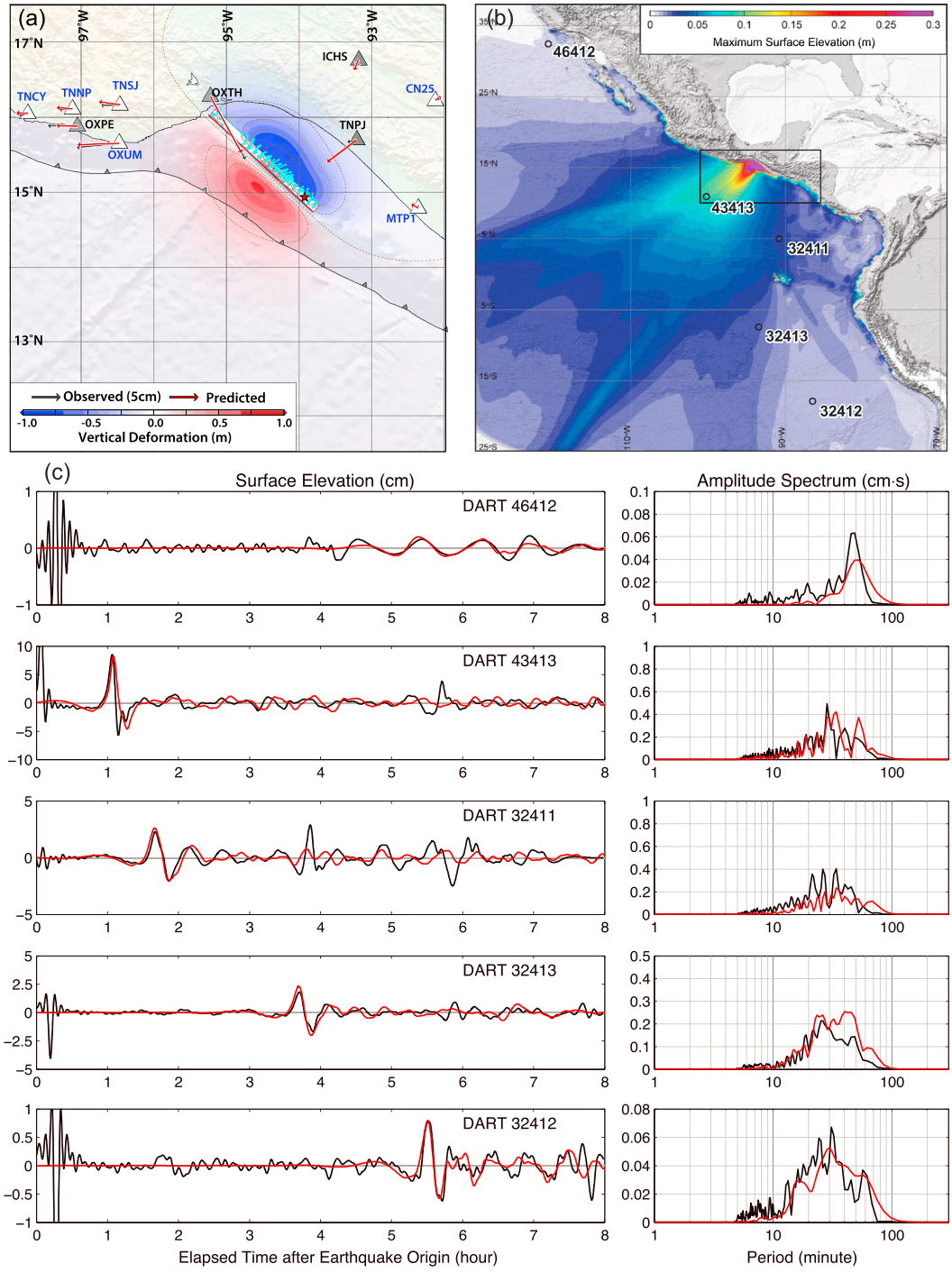

Figure 4. Comparison between observed and predicted GPS and tsunamis for our preferred slip model. (a) Black and red arrows show observed and predicted horizontal static motions at GPS stations. Background color indicates predicted vertical deformation. Data for OXPE, OXTH, ICHS, and TNPJ are determined from rapid time series with large uncertainty. The red star and rectangle show the mainshock epicenter and slip region, and cyan vectors show the slip distribution and magnitude. (b) Tsunami wave amplitude across the eastern Pacific and regional nested (black rectangle) grids at 2 arc min and 30 arc sec resolution. Circles shows the location of DART stations used in constraining the slip distribution. (c) Comparison of recorded (black) and computed (red) waveforms (left column) and amplitude spectra (right column) at DART stations.

(Figure 1a), with strike of 313° and dip of 77.7°. We found acceptable models for strike and dip varying by a few degrees, so we settled on the solution with our *W* phase geometry, ensuring consistency with long-period seismic waves as well. The moment rate function has a dominant pulse 40 s in duration, with energy later than 50 s originating near the Oaxaca coast, about 180 km from the source. The late slip abuts

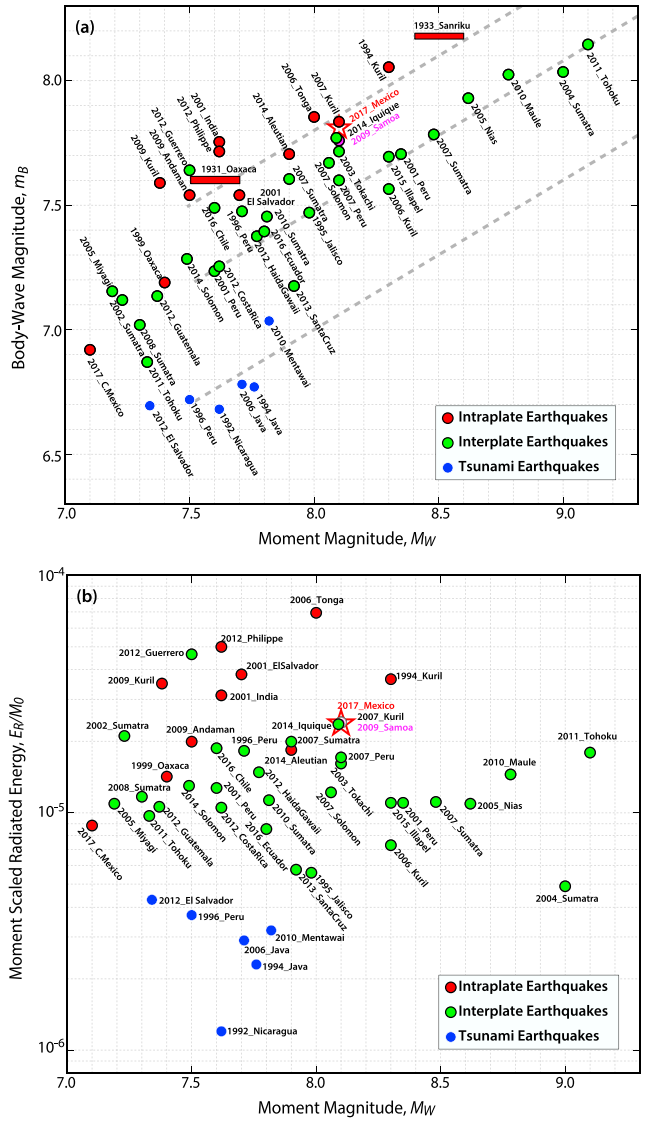

Figure 5. (a) Body wave magnitude (m_B) and (b) moment-scaled radiated energy (E_R/M_0) plotted as a function of moment magnitude (M_w) for earthquakes in different tectonic environments. The red, green, and blue dots show intraplate, typical megathrust, and tsunami earthquakes, respectively.

the edge of our model, but extending the model further overpredicts the geodetic displacements. It is plausible that the late slip is on a separate fault plane, possibly with different geometry, so it is not well constrained and is not critical to the fit of the seismic and tsunami data. However, there is certainly a need for minor slip near the coast to match the Oaxaca GPS data. The seismic moment of our final model is 2.56×10^{21} Nm, with a centroid time of 29 s, compatible with the *W* phase solution. The slip-weighted static stress drop for this model is 18 MPa using the procedure from Ye et al. (2016a).

We estimate the average source spectrum for the 2017 earthquake using the spectrum of the slip model moment rate function for frequencies less than 0.05 Hz and averaged *P* wave spectra after corrections of radiation pattern, geometrical spreading, and attenuation for higher frequencies. The decay rate, ~1.3, from ~0.1 to 1 Hz, is lower than ~1.6 average for large interplate events (Ye et al., 2016b), suggesting increased high-frequency source radiation. The radiated energy is 2.56×10^{16} J, following the procedure described by Ye et al. (2016b), giving a relatively high moment-scaled value of 2.38×10^{-5}.

3. Discussion

The seismic waves from the 2017 earthquake are relatively enriched in short-period energy, and we place the event in the context of other intraplate events relative to interplate ruptures in Figure 5. Here we determine the classic broadband body wave magnitude (m_B) (Gutenberg, 1945) measured at periods of ~3.7 s (7.79) and ~7.3 s (7.83) after converting broadband *P* waves to Wiechert seismometer responses with dominant periods of 3.5 s and 10 s, respectively, for consistency with old events (Bormann & Saul, 2009; Utsu, 2002). The 2017 event lies along the trend of m_B versus M_w for intraplate ruptures that is ~0.35 magnitude units higher than the parallel trend found for typical interplate ruptures and much higher than for tsunami earthquakes (Figure 5a). The use of the classic magnitude measure allows comparison with the 1931 Oaxaca and 1933 Sanriku normal faulting events, with the 2017 value locating on the same trend. The moment-scaled radiated energy, which can only be robustly estimated for recent events, is also consistently higher than for most interplate events (Figure 5b).

The large size of the Chiapas rupture suggests fracture of the entire Cocos lithosphere across the Tehuantepec Ridge. The lithospheric age is ~25 Ma, with ~65 km depth to the 1300°C isotherm and a brittle region ~30 km thick to the 600°C isotherm (Manea & Manea, 2006). The large-scale variation in dip of the slab may influence the stress state locally (Ponce et al., 1992), but the stress is dominated by downdip tension, consistent with the steeply dipping normal fault for the 2017 event. We view the rupture as more likely to represent breaking of the plate than bending of the upper portion of the brittle lithosphere due to the size and extent of the rupture. While the depth extent is not precisely resolved by our data, the rupture appears to extend from ~30 to 70 km, sufficient to locally detach the lithosphere. The location relative to the trench is similar to that for the 1931 Oaxaca earthquake, which is downdip of a locked portion of the megathrust (Singh et al., 1985). We infer that the seaward portion of the megathrust updip from where the 2017 rupture plane intersects it is partially locked, based on the occurrence of minor thrusting activity in this region and the regional geodetic inference of slip deficit (Franco et al., 2012). However, the lack of historic large megathrust ruptures in the relatively narrow strip of megathrust slip deficit raises the possibility that either the coupling is very heterogeneous due to the bathymetric structure of the subducting ridge, reducing the size of ruptures in the region, or the buoyancy is such that the region is undergoing high-stress creep rather than stick-slip motion. In

either case, the existence of shallow slip deficit may have concentrated slab pull stress at the lower edge of the locked zone, influencing the 2017 location, rather than allowing extensional stress to concentrate near the trench to produce great normal faulting there.

4. Conclusions

The 2017 Chiapas earthquake ruptured through the lithosphere of the subducting Cocos slab, essentially detaching the slab locally over an ~150 km long region. The event activated faulting just offshore of the Oaxaca coast on either the same fault or another one, and that signal contributed strongly to the GPS deformations in Oaxaca. The M_w 8.2 earthquake is one of the largest recorded events within a subducting plate beneath the megathrust. There are small shallow interplate thrusting events seaward of where the 2017 faulting intersects the megathrust. Along with geodetic indications of slip deficit, this suggests that the shallow slip deficit region influences where stress was concentrated to rupture within the plate. The rupture is energetic, with high moment-scaled radiated energy and a large m_B (7.8) typical of intraplate ruptures. The enhanced level of short-period energy contributed to the significant shaking damage experienced in southern Mexico.

Acknowledgments
The IRIS DMS data center (http://www.iris.edu/hq/) was used to access the seismic data from Global Seismic Network and Federation of Digital Seismic Network stations. GPS data at stations TNCY, TNNP, TNSJ, OXUM, CN25, and MTP1 are provided by Tom Herring through UNAVCO webpage (https://www.unavco.org). Data for OXPE, OXTH, ICHS, and TNPJ are determined from rapid time series from Nevada Geodetic Laboratory (http://geodesy.unr.edu). Tsunami waveform data were obtained from the NOAA National Data Buoy Center (http://www.ndbc.noaa.gov/). We thank Rob Clayton for sharing broadband data from the Mexican National Seismic Network (MX). We thank S. K. Singh for sharing his papers on normal faulting beneath Mexico. We thank X. Pérez-Campos and J. C. Castellanos for discussion about SSN aftershock locations. This work was benefitted from discussions at Seismo Lab coffee hour at Caltech. We thank G. Hayes, an anomalous reviewer, and the Editor A. V. Newman for their constructive reviews. K. D. Koper kindly provided his backprojection software. This work was supported by National Natural Science Foundation of China grants U170160005 and 41372198 to Lingling Ye and National Science Foundation grant EAR1245717 to Thorne Lay.

References

Astiz, L., & Kanamori, H. (1986). Interplate coupling and temporal variation of mechanisms of intermediate depth earthquakes in Chile. *Bulletin of the Seismological Society of America*, *767*, 1614–1622.

Astiz, L., Lay, T., & Kanamori, H. (1988). Large intermediate depth earthquakes and the subduction process. *Physics of the Earth and Planetary Interiors*, *53*(1–2), 80–166. https://doi.org/10.1016/0031-9201(88)90138-0

Bai, Y., Lay, T., Cheung, K. F., & Ye, L. (2017). Two regions of seafloor deformation generated the tsunami for the 13 November 2016, Kaikoura, New Zealand earthquake. *Geophysical Research Letters*, *44*, 6597–6606. https://doi.org/10.1002/2017GL073717

Bormann, P., & Saul, J. (2009). A fast, non-saturating magnitude estimator for great earthquakes. *Seismological Research Letters*, *80*(5), 808–816. https://doi.org/10.1785/gssrl.80.5.808

Christensen, D. H., & Lay, T. (1988). Large earthquakes associated with subduction of the Louisville Ridge. *Journal of Geophysical Research*, *93*, 13,367–13,389. https://doi.org/10.1029/JB093iB11p13367

Christensen, D. H., & Ruff, L. J. (1988). Seismic coupling and outer rise earthquakes. *Journal of Geophysical Research*, *93*, 13,421–13,444. https://doi.org/10.1029/JB093iB11p13421

DeMets, C., Gordon, R. G., & Argus, D. F. (2010). Geologically current plate motions. *Geophysical Journal International*, *181*(1), 1–80. https://doi.org/10.1111/j.1365-246X.2009.04491.x

Dmoska, R., Rice, J. R., Lovison, L. C., & Josell, D. (1988). Stress transfer and seismic phenomena in coupled subduction zones during the earthquake cycle. *Journal of Geophysical Research*, *93*, 7869–7884. https://doi.org/10.1029/JB093iB07p07869

Franco, A., Lasserre, C., Lyon-Caen, H., Kostoglodov, V., & Molina, E. (2012). Fault kinematics in northern Central America and coupling along the subduction interface of the Cocos Plate, from GPS data in Chiapas (Mexico), Guatemala and El Salvador. *Geophysical Journal International*, *189*(3), 1223–1236. https://doi.org/10.1111/j.1365-246X.2012.05390.x

Gutenberg, B. (1945). Amplitudes of *P*, *PP*, and *S* and magnitude of shallow earthquakes. *Bulletin of the Seismological Society of America*, *35*, 57–69.

Hartzell, S. H., & Heaton, T. H. (1983). Inversion of strong ground motion and teleseismic waveform data for the fault rupture history of the 1979 Imperial Valley, California, earthquake. *Bulletin of Seismological Society of America*, *73*(6A), 1553–1583.

Hayes, G., Wald, D. J., & Johnson, R. L. (2012). Slab 1.0: A three-dimensional model of global subduction zone geometries. *Journal of Geophysical Research*, *117*, B01302. https://doi.org/10.1029/2011JB008524

Kanamori, H. (1971). Seismological evidence for a lithospheric normal faulting—The Sanriku earthquake of 1933. *Physics of the Earth and Planetary Interiors*, *4*(4), 289–300. https://doi.org/10.1016/0031-9201(71)90013-6

Kanamori, H., & Rivera, L. (2008). Source inversion of *W* phase: Speeding up seismic tsunami warning. *Geophysical Journal International*, *175*(1), 222–238. https://doi.org/10.1111/j.1365-246X.2008

Kelleher, J. A., & McCann, W. R. (1976). Buoyant zones, great earthquakes, and unstable boundaries of subduction. *Journal of Geophysical Research*, *81*, 4885–4896. https://doi.org/10.1029/JB081i026p04885

Kelleher, J. A., Sykes, L. R., & Oliver, J. (1973). Possible criteria for predicting earthquake locations and their applications to major plate boundaries of the Pacific and Caribbean region. *Journal of Geophysical Research*, *78*, 2547–2585. https://doi.org/10.1029/JB078i014p02547

Kikuchi, M., & Kanamori, H. (1992). Inversion of complex body waves—III. *Bulletin of Seismological Society of America*, *81*(6), 2335–2350.

Lay, T., Astiz, L., Kanamori, H., & Christensen, D. H. (1989). Temporal variation of large intraplate earthquakes in coupled subduction zones. *Physics of the Earth and Planetary Interiors*, *54*(3–4), 258–312. https://doi.org/10.1016/0031-9201(89)90247-1

Lay, T., Kanamori, H., Ammon, C. J., Hutko, A. R., Furlong, K., & Rivera, L. (2009). The 2006–2007 Kuril Islands great earthquake sequence. *Journal of Geophysical Research*, *114*, B11308. https://doi.org/10.1029/2008JB006280

Lay, T., Ye, L., Kanamori, H., Yamazaki, Y., Cheung, K. F., Kwong, K., & Koper, K. D. (2013). The October 28, 2012 M_w 7.8 Haida Gwaii underthrusting earthquake and tsunami: Slip partitioning along the queen Charlotte fault transpressional plate boundary. *Earth and Planetary Science Letters*, *375*, 57–70.

Lynnes, C. S., & Lay, T. (1988). Source process of the great 1977 Sumba earthquake. *Journal of Geophysical Research*, *93*, 13,407–13,420. https://doi.org/10.1029/JB093iB11p13407

Manea, V. C., & Manea, M. (2006). Origin of the modern Chiapanecan volcanic arc in southern Mexico inferred from thermal models. *Geological Society of America Special Papers*, *412*, 27–38.

Mikumo, T., Yagi, Y., Singh, S. K., and Santoyo, M. A. (2002). Coseismic and postseismic stress changes in a subducting plate: Possible stress interactions between large interplate thrust and intraplate normal-faulting earthquakes, *Journal of Geophysical Research*, *107*(B1), 2023. https://doi.org/10.1026/2001JB000446

Nishenko, S. P. (1991). Circum-Pacific seismic potential: 1989–1999. *Pure and Applied Geophysics*, *135*(2), 169–259. https://doi.org/10.1007/BF00880240

Okada, Y. (1985). Surface deformation due to shear and tensile faults in a half-space. *Bulletin of Seismological Society of America*, *75*(4), 1135–1154.

Ponce, L., Gaulon, R., Suárez, G., & Lomas, E. (1992). Geometry and state of stress of the downgoing Cocos Plate in the isthmus of Tehuantepec, Mexico. *Geophysical Research Letters*, *19*, 773–776. https://doi.org/10.1029/92GL00437

Singh, S. K., Astiz, L., & Havskov, J. (1981). Seismic gaps and recurrence periods of large earthquakes along the Mexican subduction zone. *Geophysical Research Letters*, *9*, 633–636.

Singh, S. K., Ordaz, M., Alcántara, L., Shapiro, N., Kostoglodov, V., Pacheco, J. F., … Ovando, E. (2000). The Oaxaca earthquake of 30 September 1999 (M_w = 7.5): A normal-faulting event in the subducted Cocos Plate. *Seismological Research Letters*, *71*(1), 67–78.

Singh, S. K., Ordaz, M., & Pérez-Rocha, L. E. (1996). The great Mexican earthquake of 19 June 1858: Expected ground motions and damage in Mexico City from a similar future event. *Bulletin of the Seismological Society of America*, *86*, 1655–1666.

Singh, S. K., Suárez, G., & Domínguez, T. (1985). The Oaxaca, Mexico, earthquake of 1931: Lithospheric normal faulting in the subducted Cocos Plate. *Nature*, *317*(6032), 56–58. https://doi.org/10.1038/317056a0

Spence, W. (1986). The 1977 Sumba earthquake series: Evidence for Slab pull force acting at a subduction zone. *Journal of Geophysical Research*, *91*, 7225–7239. https://doi.org/10.1029/JB091iB07p07225

SSN (2017). *Servicio Sismológico Nacional*. México: Instituto de *Geofísica*, Universidad Nacional Autónoma de México. https://doi.org/10.21766/SSNMX/SN/MX

Utsu, T. (2002). Relationships between magnitude scales. *International Geophysics Series*, *81*(A), 733–746. https://doi.org/10.1016/S0074-6142(02)80247-9

Vallée, M., Bouchon, M., & Schwartz, S. Y. (2003). The 13 January 2001 El Salvador earthquake: A multidata analysis. *Journal of Geophysical Research*, *108*(B4), 2203. https://doi.org/10.1029/2002JB001922

Xu, Y., Koper, K. D., Sufri, O., Zhu, L., & Hutko, A. R. (2009). Rupture imaging of the M_w 7.9 12 May 2008 Wenchuan earthquake from back projection of teleseismic *P* waves. *Geochemistry, Geophysics, Geosystems*, *10*, Q04006. https://doi.org/10.1029/2008GC002335

Yamazaki, Y., Cheung, K. F., & Kowalik, Z. (2011). Depth-integrated, non-hydrostatic model with grid nesting for tsunami generation, propagation, and run-up. *International Journal for Numerical Methods in Fluids*, *67*(12), 2081–2107. https://doi.org/10.1002/fld.2485

Yamazaki, Y., Kowalik, Z., & Cheung, K. F. (2009). Depth-integrated, non-hydrostatic model for wave breaking and run-up. *International Journal for Numerical Methods in Fluids*, *61*(5), 473–497. https://doi.org/10.1002/fld.1952

Yamazaki, Y., Lay, T., Cheung, K. F., Yue, H., & Kanamori, H. (2011). Modeling near-field tsunami observations to improve finite-fault slip models for the 11 March 2011 Tohoku earthquake. *Geophysical Research Letters*, *38* L00G15. https://doi.org/10.1029/2011GL049130

Ye, L., Lay, T., & Kanamori, H. (2012). Intraplate and interplate faulting interactions during the august 31, 2012, Philippine trench earthquake (M_w 7.6) sequence. *Geophysical Research Letters*, *39*, L24310. https://doi.org/10.1029/2012GL054164

Ye, L., Lay, T., Kanamori, H., & Rivera, L. (2016a). Rupture characteristics of major and great ($M_w \geq 7$) megathrust earthquake from 1990–2015: 1. Moment scaling relationships. *Journal of Geophysical Research: Solid Earth*, *121*, 826–844. https://doi.org/10.1002/2015JB012426

Ye, L., Lay, T., Kanamori, H., & Rivera, L. (2016b). Rupture characteristics of major and great ($M_w \geq 7.0$) megathrust earthquakes from 1990 to 2015: 2. Depth dependence. *Journal of Geophysical Research: Solid Earth*, *121*, 845–863. https://doi.org/10.1002/2015JB012427

Geophysical Research Letters

Supporting Information for

The 2017 M_W 8.2 Chiapas, Mexico Earthquake: Energetic Slab Detachment

Lingling Ye[1,2,*], Thorne Lay[3], Yefei Bai[4], Kwok Fai Cheung[4], Hiroo Kanamori[2]

[1] Guangdong Key Lab of Geodynamics and Geohazards, School of Earth Sciences and Engineering, Sun Yat-sen University, Guangzhou, 510275, China

[2]Seismological Laboratory, California Institute of Technology, Pasadena, California, USA,

[3]Department of Earth and Planetary Sciences, University of California Santa Cruz, Santa Cruz, California, USA,

[4]Department of Ocean and Resources Engineering, University of Hawaii at Manoa, Honolulu, Hawaii, USA,

[*]Correspondence to: Lingling Ye, lingling@gps.caltech.edu

Contents of this file

Introduction

Supporting information includes 4 figures and 1 table.

Movie A1. Animation of tsunami propagation to 5 DART stations across the eastern Pacific.

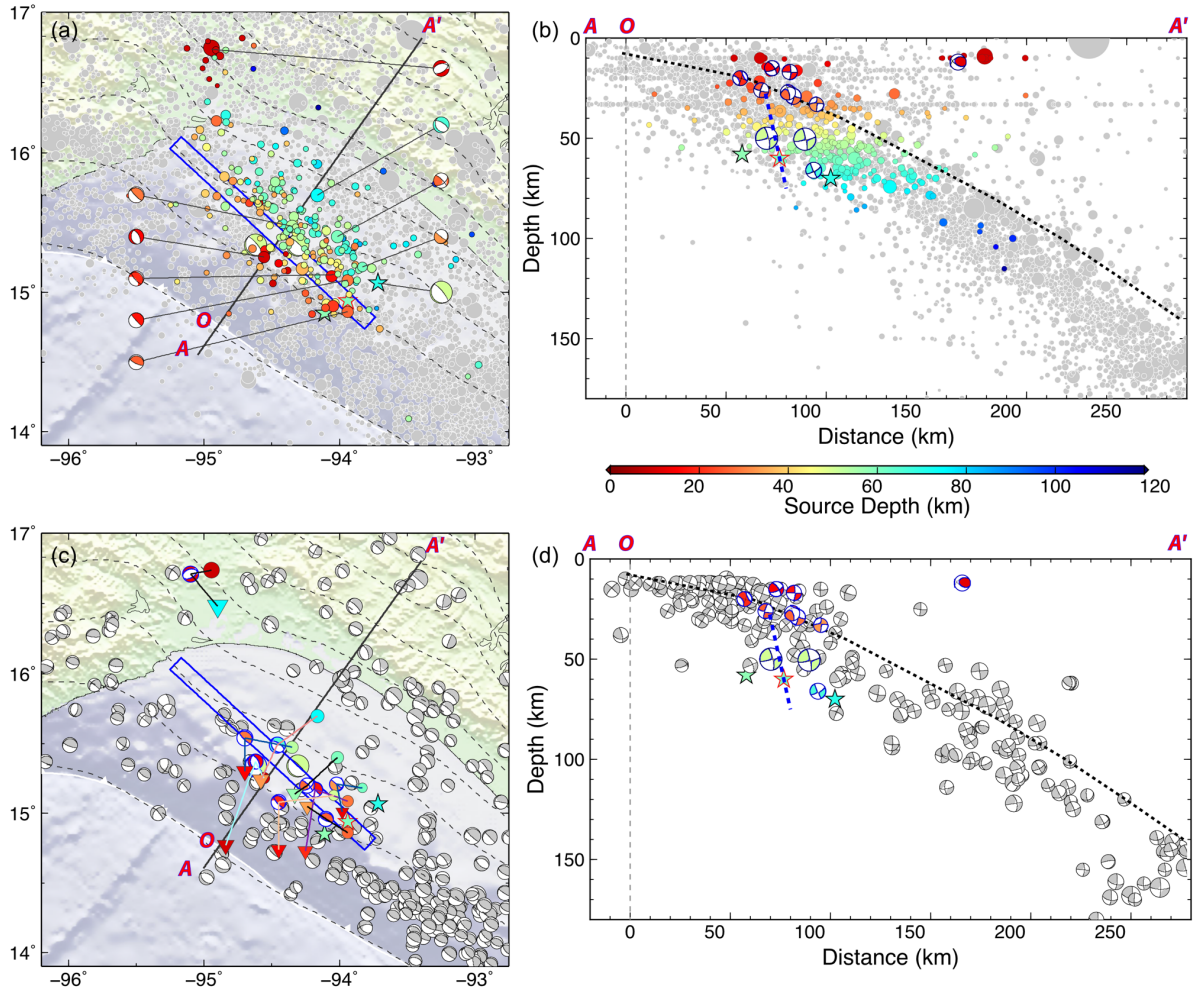

Figure S1. Seismicity around the 8 September 2017 Mw 8.1 Chiapas earthquake. (a) Historical seismicity from 1990 to 2017 (gray circles) and aftershock sequence from USGS/NEIC catalog. Focal mechanisms are global Moment-Tensor (gCMT) solutions for the mainshock (star) and aftershocks (dots). Blue rectangle indicates the slip area of the mainshock. (b) Vertical profiles of seismicity along A-A′ distances of ± 175 km in (a). Dashed blue line indicates the approximate depth extent of the mainshock. The thick dashed gray curve indicates the slab surface from the Slab 1.0 model (Hayes et al., 2012). (c) gCMT solutions for earthquakes from 1976 to 2017. Color focal mechanisms show available aftershocks from the gCMT catalog, with bars connecting to USGS/NEIC epicenter (circles) and to Mexico SSN catalog (triangles). It shows that earthquakes are relocated systematically more landward in the USGS/NEIC catalog, whereas they are more toward the trench in the SSN catalog for this region, as compared to the gCMT location. (d) Vertical profiles like (b), but for the gCMT mechanism in (c).

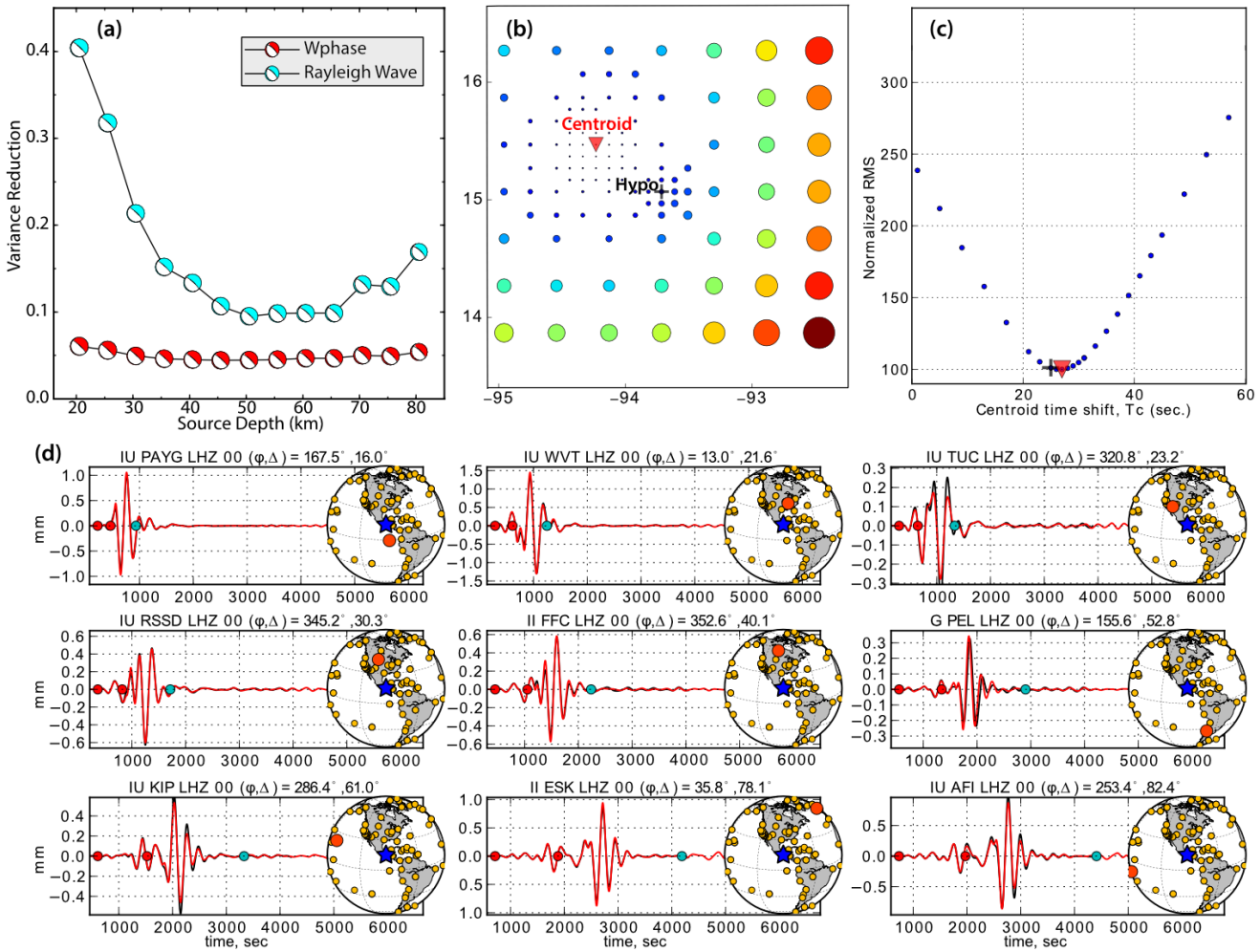

Figure S2. Long-period point-source moment tensor solution for the 2017 Chiapas earthquake. (a) Residual waveform variance of W-phase moment tensor inversions (red) using three-component observations in the period range 200–500 s for varying assumed source depths. The cyan focal mechanisms show the residual waveform variance for predicted vertical component Rayleigh waves (5-200s) for the W-phase solution at each source depth. (b) and (c) Grid search of centroid location and centroid time shift with depth at 50.5 km respectively. Circles in (b) are scaled with normalized root mean square (RMS) misfit of W-phase waveforms. (d) Example W-phase waveforms (between red dots) and Rayleigh waves (between 2nd and 3rd dots) for observations (black) and computed waveforms (red) for the point-source moment tensor solution at 50.5 km. The maps indicate the position of each station (red circle) among the total set of stations used in the W-phase inversion (gold circles). Comparable waveform matches are found for all the stations indicated in the maps.

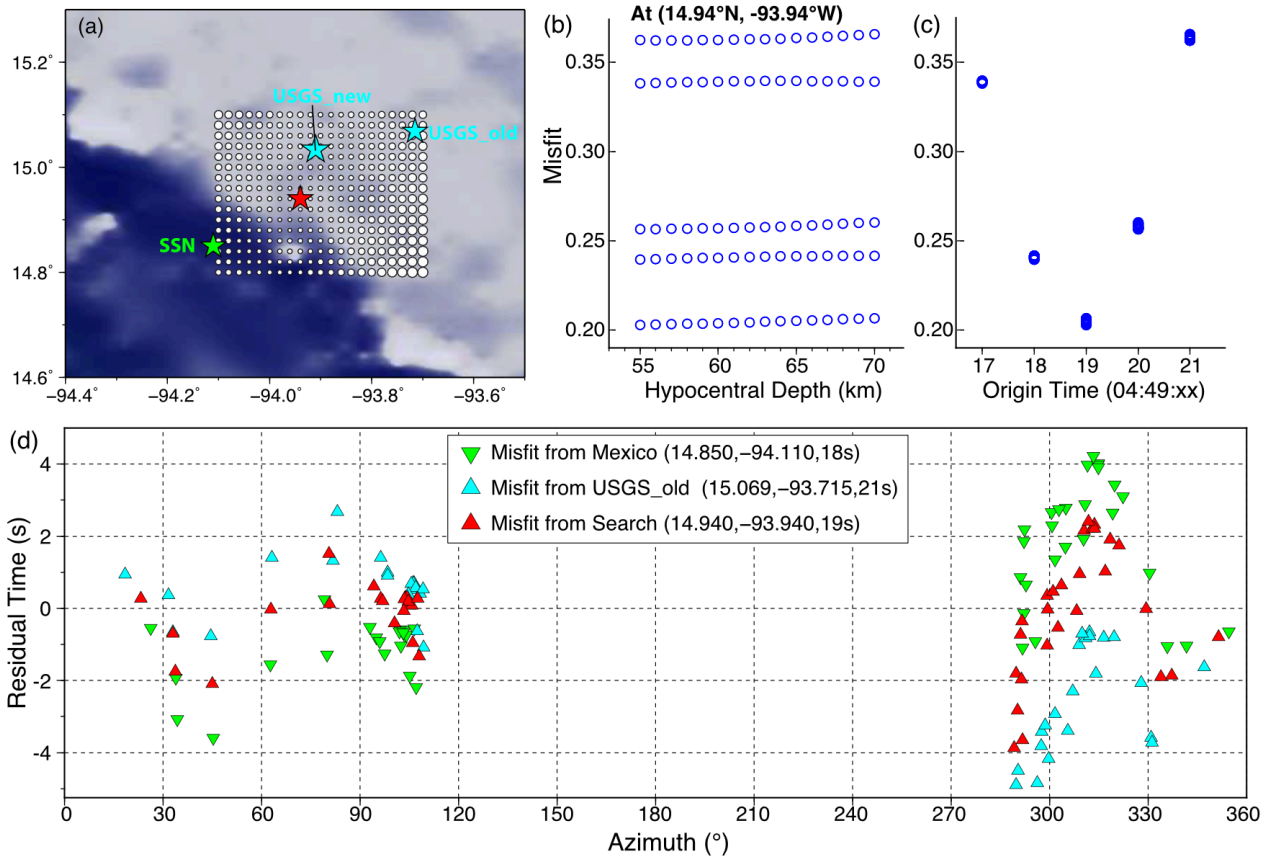

Figure S3. Relocation of the hypocenter and origin time for the 2017 Chiapas earthquake using hand-picked P-wave arrivals in vertical component stations within 10° for IRIS and seismic networks in Mexico (SSN, 2017). (a) Map view of misfit of P arrivals for variable assumed epicenter locations (gray dots). Dots are scaled with the misfit. The cyan, green and red stars show the epicenters from USGS-NEIC catalog (both initial and updated ones), Mexico SSN catalog from National Autonomous University of Mexico (http://www.ssn.unam.mx/) and the relocated position, respectively. (b) Misfit variation with varying assumed hypocenter depths at the preferred epicenter. Different rows correspond to different original times. (c) Misfit variation with varying assumed origin times. (d) Residuals of observed P arrival times from predicted values with hypocenter and origin time from Mexico SSN catalog (green triangles), USGS/NEIC catalog (cyan triangles, initial USGS location), and our relocated solution (red triangles).

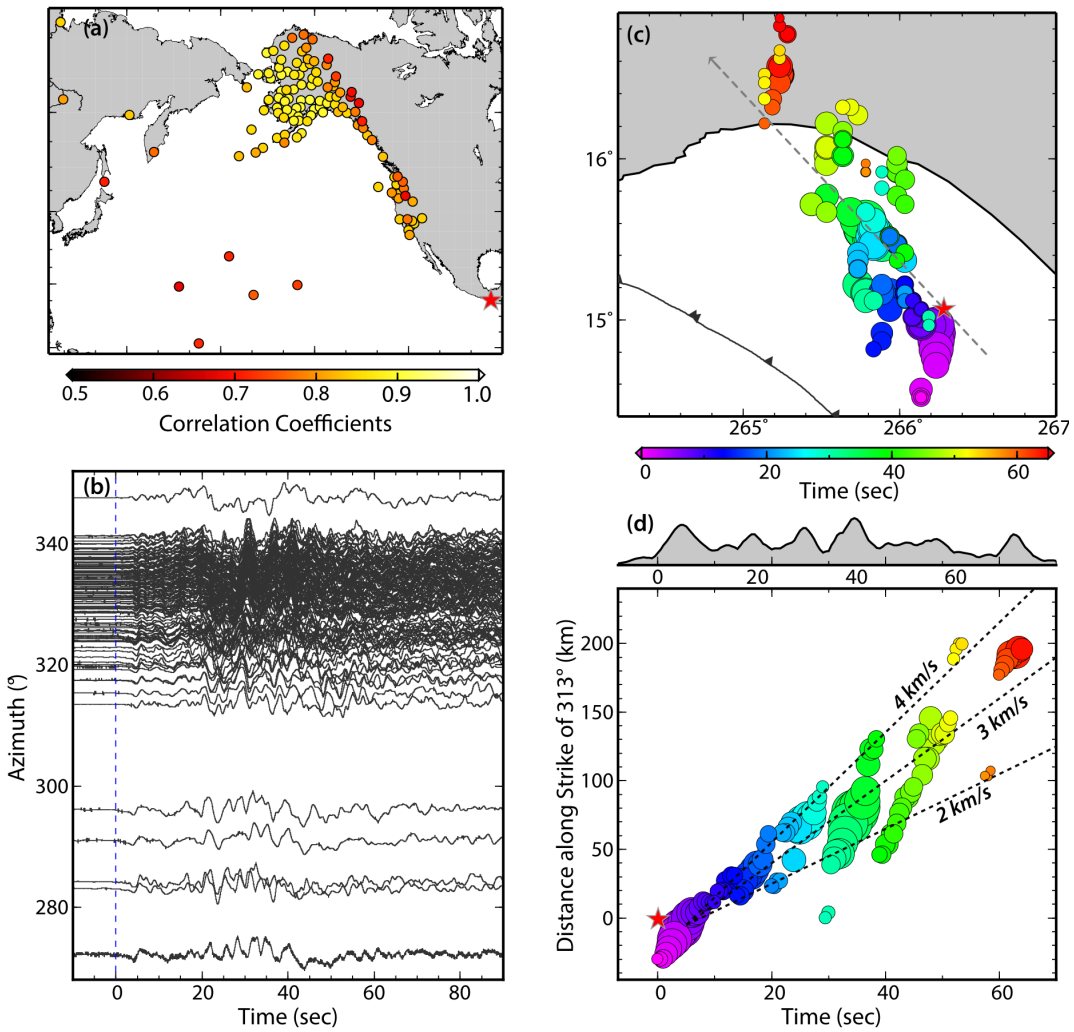

Figure S4. Back-projection (BP) image of short-period (0.5-2.0 Hs) teleseismic P waves for the 2017 Chiapas earthquake. (a) Distribution of stations used in the BP image, color-coded by correlation coefficients of Multiple-Component Cross Correlation (MCCC) of initial P waves for time windows from 5 s before to 5 s after predicted P arrivals for model AK135. The red star is the epicenter of the 2017 Chiapas earthquake from the USGS/NEIC catalog. (b) Aligned waveforms of teleseismic P records using MCCC. Each trace is self-normalized. (c) Map view of large stack peaks in 5 s time windows, color-coded by the central time of each time window. (d) Linear time and distance plot of large peaks. The distance is projected along the fault strike direction with azimuth of 313°. This BP image indicates a dominant unilateral rupture propagation toward the northwest from the epicenter with speed of ~ 3.0 to 3.5 km/s.

Table S1. Crustal structure used for teleseismic inversion.

Vp (km/s)	Vs (km/s)	Density (g/cm^3)	Thickness (km)
1.50	0.00	1.02	0.2
2.30	1.10	2.20	1.5
3.20	1.60	2.30	0.5
6.00	3.40	2.70	7.0
6.60	3.70	2.90	7.0
7.20	4.00	3.05	7.0
7.90	4.56	3.30	70.0
8.00	4.57	3.31	half space